

Subarcsecond international LOFAR radio images of the M82 nucleus at 118 MHz and 154 MHz

E. Varenius¹, J. E. Conway¹, I. Martí-Vidal¹, R. Beswick², A. T. Deller³, O. Wucknitz⁴, N. Jackson², B. Adebahr⁴, M. A. Pérez-Torres^{5,6,7}, K. T. Chyży⁸, T. D. Carozzi¹, J. Moldón³, S. Aalto¹, R. Beck⁴, P. Best⁹, R.-J. Dettmar¹⁰, W. van Driel¹¹, G. Brunetti¹², M. Brügger¹³, M. Haverkorn^{14,15}, G. Heald^{3,16}, C. Horellou¹, M. J. Jarvis^{17,18}, L. K. Morabito¹⁵, G. K. Miley¹⁵, H. J. A. Röttgering¹⁵, M. C. Toribio³, and G. J. White^{19,20}

¹ Department of Earth and Space Sciences, Chalmers University of Technology, Onsala Space Observatory, 439 92 Onsala, Sweden
 e-mail: varenius@chalmers.se

² Jodrell Bank Centre for Astrophysics, Alan Turing Building, School of Physics and Astronomy, The University of Manchester, M13 9PL Manchester, UK

³ The Netherlands Institute for Radio Astronomy (ASTRON), PO Box 2, 7990 AA Dwingeloo, The Netherlands

⁴ Max-Planck-Institut für Radioastronomie, Auf dem Hügel 69, 53121 Bonn, Germany

⁵ Instituto de Astrofísica de Andalucía, Glorieta de las Astronomía, s/n, 18008 Granada, Spain

⁶ Centro de Estudios de la Física del Cosmos de Aragón, 44001 Teruel, Spain

⁷ Departamento de Física Teórica, Facultad de Ciencias, Universidad de Zaragoza, 50009 Zaragoza, Spain

⁸ Obserwatorium Astronomiczne Uniwersytetu Jagiellońskiego, ul. Orła 171, 30-244 Kraków, Poland

⁹ SUPA, Institute for Astronomy, Royal Observatory Edinburgh, Blackford Hill, EH9 3HJ Edinburgh, UK

¹⁰ Ruhr-Universität Bochum, Astronomisches Institut, 44780 Bochum, Germany

¹¹ GEPI, Observatoire de Paris, CNRS, Université Paris Diderot, 5 place Jules Janssen, 92190 Meudon, France

¹² INAF-Istituto di Radioastronomia, via P. Gobetti 101, 40129 Bologna, Italy

¹³ Hamburger Sternwarte, University of Hamburg, Gojenbergsweg 112, 21029 Hamburg, Germany

¹⁴ Department of Astrophysics/IMAPP, Radboud University, PO Box 9010, 6500 GL Nijmegen, The Netherlands

¹⁵ Leiden Observatory, Leiden University, PO Box 9513, 2300 RA Leiden, The Netherlands

¹⁶ Kapteyn Astronomical Institute, Postbus 800, 9700 AV Groningen, The Netherlands

¹⁷ Astrophysics, Department of Physics, Keble Road, OX1 3RH Oxford, UK

¹⁸ Department of Physics, University of the Western Cape, Private Bag X17, 7535 Bellville, South Africa

¹⁹ Department of Physical Sciences, The Open University, MK7 6AA Milton Keynes, UK

²⁰ RALSpace, The Rutherford Appleton Laboratory, Chilton, Didcot, OX11 0NL Oxfordshire, UK

Received 1 October 2014 / Accepted 26 November 2014

ABSTRACT

Context. The nuclear starburst in the nearby galaxy M82 provides an excellent laboratory for understanding the physics of star formation. This galaxy has been extensively observed in the past, revealing tens of radio-bright compact objects embedded in a diffuse free-free absorbing medium. Our understanding of the structure and physics of this medium in M82 can be greatly improved by high-resolution images at low frequencies where the effects of free-free absorption are most prominent.

Aims. The aims of this study are, firstly, to demonstrate imaging using international baselines of the Low Frequency Array (LOFAR), and secondly, to constrain low-frequency spectra of compact and diffuse emission in the central starburst region of M82 via high-resolution radio imaging at low frequencies.

Methods. The international LOFAR telescope was used to observe M82 at 110–126 MHz and 146–162 MHz. Images were obtained using standard techniques from very long baseline interferometry. Images were obtained at each frequency range: one only using international baselines, and one only using the longest Dutch (remote) baselines.

Results. The 154 MHz image obtained using international baselines is a new imaging record in terms of combined image resolution (0.3'') and sensitivity ($\sigma = 0.15$ mJy/beam) at low frequencies (<327 MHz). We detected 16 objects at 154 MHz, six of these also at 118 MHz. Seven objects detected at 154 MHz have not been catalogued previously. For the nine objects previously detected, we obtained spectral indices and emission measures by fitting models to spectra (combining LOFAR with literature data). Four weaker but resolved features are also found: a linear (50 pc) filament and three other resolved objects, of which two show a clear shell structure. We do not detect any emission from either supernova 2008iz or from the radio transient source 43.78+59.3. The images obtained using remote baselines show diffuse emission, associated with the outflow in M82, with reduced brightness in the region of the edge-on star-forming disk.

Key words. techniques: interferometric – techniques: high angular resolution – supernovae: individual: 2008iz – galaxies: starburst – galaxies: individual: M82 – galaxies: star formation

1. Introduction

The nearby (3.52 ± 0.02 Mpc; [Tully et al. 2009](#)) galaxy M82 is one of the most studied extragalactic sources across the electromagnetic spectrum. In the radio band, M82 has been

observed in a wide range of spatial resolutions in both the continuum and the spectral line. Multiple radio-emitting compact objects were first discovered and confirmed in the nucleus more than 30 years ago ([Kronberg et al. 1972](#); [Unger et al. 1984](#)). To date, high-resolution continuum observations have revealed

more than 50 compact objects thought to be radio supernovae (SNe), supernova remnants (SNRs) or HII-regions (Gendre et al. 2013). The M82 nucleus provides an excellent laboratory for studying the physics of these compact objects and the internal medium in which they are embedded. Optical observations (Westmoquette et al. 2009) show that the ionised gas in the starburst core of M82 is dynamically complex. The properties of the absorbing ionised gas component in M82 can be studied by its low-frequency free-free absorption of continuum emission. A key motivation of such observations is to determine the structure of the absorbing medium; uniform or “clumpy” (Lacki 2013). Evidence of clumpy free-free absorption has been found in many galaxies using low-frequency observations (Israel & Mahoney 1990; Israel et al. 1992). Detailed modelling of SNR evolution at low frequencies is also important for improving understanding of cosmic ray injection in galaxies.

The integrated low-frequency radio spectrum of M82 has been studied for more than 20 years (Condon 1992). Recently, M82 has been imaged at 327 MHz ($\lambda = 92$ cm) with 40'' resolution using the Westerbork synthesis radio telescope (WSRT) by Adebahr et al. (2013), observations that show a radio-bright extended halo structure for M82. However, imaging with resolution of tenths of an arcsecond is required to properly study the compact objects at low frequencies.

Pioneering subarcsecond observations were done in the 1960s using very long baseline interferometry to probe angular scales as small as 0.1'' in bright objects such as Jupiter (e.g. Carr et al. 1970; Clark et al. 1975). However, these observations were limited to measuring sizes (or upper limits) using visibility amplitude information and no imaging was performed.

Imaging with subarcsecond resolution has been carried out at 327 MHz by, amongst others, Wrobel & Simon (1986), Ananthakrishnan et al. (1989) and Lenc et al. (2008), using international and intercontinental baselines. At lower frequencies, imaging has been performed with arcsecond resolution, for example using the 151 MHz ($\lambda = 2$ m) system installed on the Multi-Element Radio Linked Interferometer Network (MERLIN) in the mid-to-late 1980s (Leahy et al. 1989), which had baselines up to 217 km but could only record a narrow bandwidth (typically 1 MHz).

Low-frequency turnovers in SNR spectra have been used to study the clumpy absorbing medium in our galaxy in detail (see e.g. Kassim 1989). Pioneering very high resolution (0.5'') observations of M82 by Wills et al. (1997) using MERLIN at 408 MHz ($\lambda = 74$ cm) have shown evidence of low-frequency turnovers in the spectra of multiple compact objects in M82, which is mainly attributed to free-free absorbing gas.

However, for many objects, the low-frequency spectra are not well constrained, and some may have spectral turnovers well below 408 MHz. To investigate such objects, as well as to potentially detect new classes of very steep spectrum compact sources, requires high-resolution observations at lower frequencies. Achieving a few tenths of an arcsecond resolution, as required to separate compact sources from diffuse emission, needs 1000 km baselines and hence the international baselines of the Low Frequency Array (LOFAR). International LOFAR baselines are only sensitive to very compact objects, which in M82 are weaker than the strong (>10 Jy) extended radio emission seen at shorter baselines towards the centre of the galaxy. The above scientific goals and its high declination make M82 an excellent target for demonstrating international LOFAR imaging on a weak but complex target source. Observations using the international baselines of LOFAR are not yet a regularly used mode. Pioneering work using the low band (30–80 MHz)

succeeded in imaging the source 3C 196 with a resolution of $\sim 1''$ only using a fraction of the final array (Wucknitz 2010b). This commissioning continued in the high band (110–190 MHz), where a resolution of 0.3'' was achieved for a number of bright and compact sources (Wucknitz 2010a). The LOFAR community have concluded that standard very long baseline interferometry (VLBI) techniques can be used to produce high-resolution images from LOFAR observations. Several unpublished high-band observations of Jansky level sources have been made and multiple observations including international LOFAR baselines have been scheduled in LOFAR cycles 0, 1 and 2.

In this paper, we present subarcsecond images of the nuclear starburst in M82 at central frequencies of 118 MHz ($\lambda = 2.5$ m) and 154 MHz ($\lambda = 1.9$ m), made using international LOFAR baselines, thereby setting a new record in terms of combined image resolution and point source sensitivity for science images at frequencies below 327 MHz. The contents of this paper are as follows: in Sect. 2 we describe in detail the observational setup and calibration procedures applied to the LOFAR data. This section also briefly describes the eMERLIN data used for comparison throughout this paper. In Sect. 3, we describe how images were obtained from LOFAR data and summarise the calibration and imaging procedures. In Sect. 4, we present the images obtained and briefly discuss our results in relation to previous work. Finally, we summarise our conclusions in Sect. 5. A more extensive scientific discussion regarding the compact and extended emission in M82 will be the subject of a forthcoming paper. Throughout this paper we adopt a distance to M82 of 3.52 Mpc (Tully et al. 2009) so that 1'' corresponds to 17 pc.

2. Data and calibration

In this section, we describe the two data sets used in this paper and the processing done for obtaining images. In particular, we describe in detail the processing done to image the international LOFAR baselines, since our strategy differs from what is usually done to image shorter LOFAR baselines.

2.1. eMERLIN data

The eMERLIN data set was observed on January 20th 2014 at 1.6 GHz, under project code CY1203 (P.I.: Pérez-Torres), with additional observations taken in collaboration with the LeMMINGs e-MERLIN legacy project (P.I.: Beswick & McHardy). These data were calibrated and imaged in a standard way by eMERLIN staff. Since these data are only used for comparison in this paper, we refer any details on the calibration to the paper describing these data, see Pérez-Torres et al. (2014).

2.2. LOFAR data

Our project LC0_026 (P.I.: J.E. Conway) was observed in two parts to maximise hour angle coverage during night time: 10 h taken during the night between the 20, and 21, March 2013 (in UT range 16:15–02:45) and six hours taken in the evening of April 5, 2013 (in UT range 17:45–00:15 UT). Both the March and April observations included the same 44 LOFAR high band antenna (HBA) stations: 23 core stations (CS), 13 remote stations (RS), and eight international (INT) stations. Participating INT stations were DE601, DE602, DE603, DE604, DE605, FR606, SE607, UK608, although no fringes were detected to DE604.

Table 1. Correlation positions for each beam.

Source	RA [J2000]	Dec [J2000]
3C 196 ^a	08h13m36.0000s	48°13′03″000
J0958+6533 ^b	09h58m47.2451s	65°33′54″818
M81* ^c	09h55m33.1731s	69°03′55″062
M82 ^d	09h55m51.5500s	69°40′45″792

Notes. ^(a) From NED (<http://ned.ipac.caltech.edu>). ^(b) From the VLBA Calibrator list (<http://www.vlba.nrao.edu/astro/calib>). ^(c) Centred on the core M81* (Bietenholz et al. 2004; Martí-Vidal et al. 2011b). ^(d) Centred on supernova SN2008iz in M82 (Brunthaler et al. 2009).

This experiment was designed to observe, as targets, both the active galactic nucleus (AGN) in M81 (hereafter M81*) and the nucleus of the galaxy M82; these two objects are only separated by 0.61° on the sky (scientific results on M81* will be presented in a future paper). Three objects, J0958+6533 (hereafter J0958), M81* and M82, were observed simultaneously using three beams. Even though M81* and M82 lie within the width of a single HBA station beam, the field of view (FOV) of international baseline observations is limited by frequency and time averaging effects (see below), so that two separate correlation phase centres were needed. The source J0958, at angular distance of 3.5° from M81* and 4.1° from M82, was used as a calibrator of fringe-rate and delay. This source is listed in the VLBA calibrator list as a compact source and was known to have a flux density of 0.86 Jy at 73.8 MHz in VLSSr (Lane et al. 2014). M81* was observed both as a scientific target and as a close phase calibrator for M82. Every hour, the observations switched to a single beam on 3C 196 for two minutes. 3C 196 was observed to anchor the absolute flux scale of the observations. The positions assumed for correlation and calibration of each source are listed in Table 1.

Data were taken in 8-bit HBA joined mode, where the data from each HBA subfield (or “ear”) in a CS are combined at the station level. The available total bandwidth of 96 MHz was divided equally between the three beams on M81*, M82 and J0958. The single beam on 3C 196 covered the same 32 MHz. The observed 32 MHz bandwidth per beam was divided into two contiguous blocks of 16 MHz each, one centred on 118 MHz and one centred on 154 MHz. The lower frequency block was chosen to include the lowest frequencies observable with the HBA, and the higher frequency range was placed in the region with the highest HBA sensitivity. The two blocks were calibrated separately but following the same procedure.

The data were correlated producing all four linear polarisation products (XX, XY, YX, YY). After correlation, the data were stored in the LOFAR long term archive (LTA) as measurement sets (MS) with integration time 1.0 s and 64ch/sub-band, corresponding to a channel resolution of 3 kHz. In addition to the raw high-resolution data, the LOFAR pipeline was used to automatically edit bad data, and save the edited data set averaged in time and frequency down to 2 s integration time and 4ch/sub-band (giving a channel width of 48 kHz). These averaged data were saved in the LOFAR long term archive (LTA). Inspection of data for the bright calibrator J0958 revealed that ionospheric phase errors varied slowly enough over time and frequency to enable further averaging without significant coherence losses. To speed up the processing the data were therefore finally averaged, using the LOFAR *new default pre-processing pipeline* (NDPPP), to 10.0 s integration time and 1 ch/sb (channel width 195 kHz).

At this point the total data volume was reduced to 170 GB for each of the two frequency blocks.

2.2.1. Baseline definitions and coherence losses

The international LOFAR telescope provides a very good sampling of Fourier space covering baselines of lengths between 0.1 k λ and 550 k λ (except for a gap between 35 k λ and 65 k λ) at 118 MHz, and between 0.1 k λ and 700 k λ (except for a gap between 45 k λ and 80 k λ) at 154 MHz¹. In this paper we present images made using Dutch (remote) baselines and international baselines. At these frequencies, remote baselines are baselines of length between 2 k λ and 60 k λ . International baselines are defined as longer than 60 k λ .

Given the final spectral and temporal resolution of the data (10.0 s 1 ch/sb), we estimate the coherence loss due to time and frequency smearing at an angular distance of $30''$ from the phase centre to be less than 3% for the longest international (1158 km) baseline. This estimate includes a simple upper bound for time smearing assuming the source to be at the celestial north pole. Similarly, we estimate the coherence loss to be less than 3% for the longest Dutch remote baselines (121 km) for emission at an angular distance of $5'$ from the centre. Including residual rates and delays (typically 3 mHz and 300 ns) present when averaging the data we estimate a total coherence loss of less than 5%. Hence, we may image a field of $1'$ around the central M82 position using INT baselines and $10'$ using RS baselines, without significant loss due to averaging.

2.2.2. Correcting for residual delay, rate and phase

Because of residual rates affecting international baselines we need to derive rate corrections using a global fringe-fitting algorithm. This has not yet been implemented within the LOFAR software packages, nor in the Common Astronomy Software Applications (CASA) 4.2.1 (McMullin et al. 2007). Therefore, we decided to use Astronomical Image Processing System (AIPS) 31DEC13 (Greisen 2003) and ParselTongue 2.0 (Kettenis et al. 2006), to calibrate these data.

Distortion of the signal due to the ionosphere is challenging to remove in a linear (X, Y) polarisation basis, since both amplitudes and phases are affected in a coupled way. To simplify the problem, we convert to a circular (R, L) polarisation basis, where the ionospheric disturbance is transformed to phase-only effects, and employ standard VLBI techniques. Since Faraday rotation does not mix R and L polarisations we may calibrate RR and LL independently. Hence, in a circular basis, corrections for phase and amplitude can be derived independently. The data were converted from linear to circular polarisation using the tool *mscor-pol* v1.6, developed by T. Carozzi. This tool includes corrections for dipole-projection effects as a function of the correlated sky position relative to all included LOFAR stations. After the conversion, the data are circularly polarised, with full (but approximated) parallactic angle correction. The data were then converted to UVFITS format using the task *exportuvfits* in CASA and read into AIPS.

Before further processing, the task FIXWT was used to set the relative weights of all visibilities to the inverse square of the standard deviation within five minutes of data. Hence, the relative weights should reflect the scatter of the data.

¹ This gap will be largely filled when the final Dutch remote stations are operational.

The global fringe fitting algorithm (Thompson et al. 2001), as implemented in the AIPS task FRING, only solves for a single residual delay within each intermediate frequency (IF). At low radio frequencies, the residual delay due to the ionosphere varies considerably as a function of frequency. Since these data cover a large fractional bandwidth (10%), solving for one single delay over the full 16 MHz might leave significant residual delays in parts of the spectrum. To mitigate this effect, each 16 MHz block (of 81 channels) was split in three groups (“IFs” in AIPS) of 27 channels each, using the task MORIF.

Corrections for residual delays and rates were derived using J0958. The search was restricted to baselines longer than 60 k λ , a delay search window of 600 ns, a rate search window of 30 mHz, and a solution interval of two minutes. Solutions were found separately for each IF and polarisation. Since all CS are close and share a common clock, no corrections were needed for the core stations, only for the INT and RS. Typical residual delays were found to be 100–300 ns, and typical residual rates were 1–3 mHz. To correct a few obvious outliers, the corrections were filtered using a median window filter before applying them to the data. The difference in residual delay between the lowest and highest frequencies of the three IFs were typically 10–15 ns for the international stations. Bad data were edited using UVFLG in AIPS. No fringes were detected to DE604 and this station was not used in the imaging. We note that the problems with DE604 have been fixed since these data were taken.

2.2.3. Setting the absolute flux scale

After correcting for residual delays and rates, the task CALIB was used to derive amplitude and phase corrections for J0958, assuming this source to be a 0.5 Jy flat-spectrum point source at the phase centre. A solution interval of two minutes was used together with the “L1-norm” option, and the two circular polarisations were averaged to form a single solution for both polarisations.

J0958 is compact, but there is another strong (0.5 Jy) source nearby (distance 4.7' north of J0958). Only baselines >60 k λ were used when determining amplitude corrections, thereby limiting the field of view around J0958 because of smearing, which means avoiding any disturbing interference from this source. For clarity we emphasise that the amplitude corrections are derived for all stations, INT, RS, and CS, but only using the longest baselines. The solutions and final corrected visibilities were inspected to ensure that good solutions were found. After applying the corrections, imaging using task IMAGR in AIPS recovered a compact source of 498 mJy at 118 MHz and 502 mJy at 154 MHz (using baselines >60 k λ , pixel size 0.02" and robust 0 weighting;) in good agreement with what was specified. Flux densities are given as reported by fitting Gaussian intensity distributions using JMFIT in AIPS. The CLEAN restoring beam was 0.48" \times 0.33", rms noise σ = 0.4 mJy/beam at 118 MHz, and 0.36" \times 0.23", rms noise σ = 0.2 mJy/beam at 154 MHz. In addition to the compact source, a weak 5" extension can be seen to the southwest (see Fig. 1 made using the multi-scale option in CASA to better deconvolve extended emission). This southwest extension is known from previous observations at 1.4 GHz by Xu et al. (1995). Since the point source is 100 times brighter than the extension, a point source model is sufficiently accurate to determine calibration solutions. In case the extended structure has introduced minor phase errors, these will be corrected using M81* before imaging of M82.

Imaging using baselines between 2 and 60 k λ (i.e. excluding baselines to INT stations as well as CS-CS) we recover

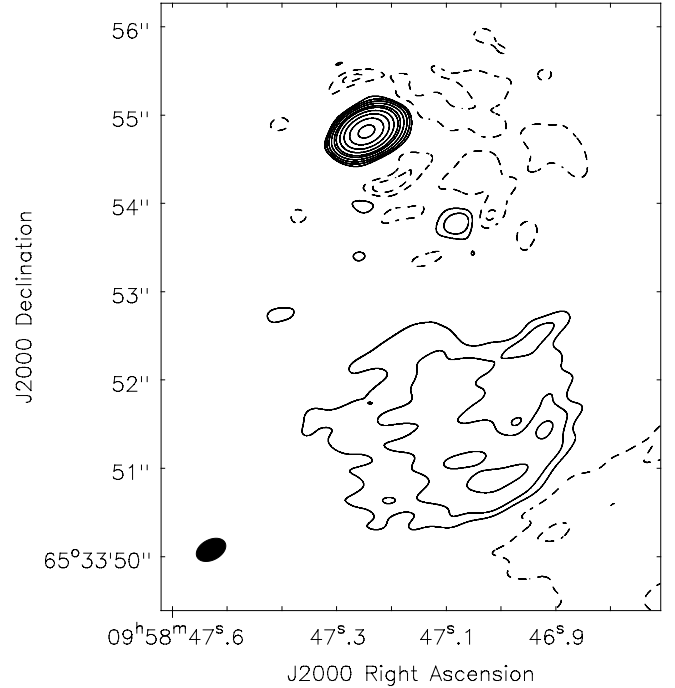


Fig. 1. Calibrator J0958+6533 at 154 MHz using baselines longer than 60 k λ . The rms noise is σ = 0.2 mJy/beam. The beam of 0.36" \times 0.23" is shown in the bottom left. The contour levels are $(-10, -5, 5, 10, 20, 40, 80, 125, 250, 500, 1000, 2000) \times \sigma$. A southwest extension is clearly visible, although the point source is 100 times brighter than the extension. This image was obtained using the multi-scale option in CLEAN (CASA 4.2.1) with scales = [0, 40, 80, 160] pixels, with pixel size 0.02".

686 mJy with a peak of 592 mJy/beam at 118 MHz (CLEAN beam 6.35" \times 5.37", pixel size 0.5", σ = 0.33 mJy/beam) and 646 mJy with a peak of 549 mJy/beam at 154 MHz (CLEAN beam 5.07" \times 4.34", pixel size 0.5", σ = 0.14 mJy/beam). It is clear that J0958 is partially resolved at these frequencies and the integrated flux density recovered is hence a lower limit. We note that the integrated flux density recovered at 73.8 MHz of 860 mJy (Cohen et al. 2007, VLSSr beam 75") is 25% higher than found here at 118 MHz.

To check the flux scale, the cumulative corrections derived for J0958 were applied to 3C 196. Because of the large angular separation (22°) of 3C 196 with respect to J0958, the phase calibration was refined for 3C 196 using the CS and RS, assuming a point source model and deriving one solution for each 2 min scan. The corrections were found using baselines in the range 0.1 to 60 k λ (excluding the shortest CS baselines as well as INT baselines). The two polarisations were averaged together, but each IF was solved separately.

We note that 3C 196 is resolved at the RS baselines, but still compact enough for a point source model to work for phase calibration. Because of the limited Fourier sampling (16 \times 2 min) we did not calibrate and image the INT station visibilities of 3C 196. However, this was not necessary to obtain the integrated flux densities at 118 and 154 MHz. For clarity we emphasise that no corrections derived for 3C 196 were transferred to any other source; 3C 196 was just imaged to check the amplitude calibration. The amplitude corrections for all stations were derived using J0958. We also note that no beam corrections were made in addition to what was applied by *mscorpol*. Because of the small field of view imaged in this work, any residual beam

errors should have a very minor impact. This calibration strategy is different (and simpler) than what is normally used when imaging wide fields (where the field of view is comparable to the station beam) with LOFAR.

Imaging of 3C 196 was done using baselines of length 0.1–60 k λ , pixel size 0.2'' and robust 0 weighting. The resulting images recover 102.0 Jy at 118 MHz (CLEAN beam 7.37'' \times 5.40'', σ = 0.3 Jy/beam) and 84.2 Jy at 154 MHz (CLEAN beam 7.57'' \times 5.95'', σ = 0.1 Jy/beam).

We estimate our absolute flux calibration to be accurate to within 10%. With this in mind, the recovered flux densities for 3C 196 are in excellent agreement with the 98.0 Jy and 81.6 Jy expected at 118 MHz and 154 MHz respectively from the best-fit model for 3C 196 derived by [Scaife & Heald \(2012\)](#).

2.2.4. Refining the phase calibration using M81*

We found M81* to be too weak to determine delay and rate corrections using FRING. Approximating the ionosphere as a simple slab, and assuming a typical observing elevation of 60° and a typical delay in direction of J0958 as 200 ns, we estimate the delay difference over the 3.5° angular separation on the sky between J0958 and M82* to be 10 ns. This would, given the full 16 MHz bandwidth, introduce a coherence loss of 1.8% when averaging all channels for M81 and M82. We find this acceptable and cumulative corrections derived for J0958 (delay, rate, amplitude and phase) were transferred to M81*. Because of the angular separation between J0958 and M81* it was necessary to do phase-only calibration on M81* to derive additional phase corrections towards M81*. A point-source model was used and corrections were derived using baselines >60 k λ , averaging over IFs and polarisation. At 118 MHz corrections were derived every four minutes, and at 154 MHz corrections were derived every two minutes.

Deconvolved images of M81* were obtained using the AIPS task IMAGR. Using baselines between 2 and 60 k λ and pixel size 0.5'' we recover 67.9 mJy with a peak of 52.1 mJy/beam at 118 MHz (CLEAN beam 6.22'' \times 5.17'' σ = 0.37 mJy/beam), and 68.6 mJy with a peak of 52.7 mJy/beam at 154 MHz (CLEAN beam 4.92'' \times 4.05'', σ = 0.16 mJy/beam). Since the peak flux density is smaller than the integrated flux density it is clear that M81* is partially resolved at both frequencies using RS baselines. Most of the flux comes from a compact (5'') central source. There is a hint of emission extending up to 10'' from the centre but this could also be a result of cleaning artefacts. Using baselines >60 k λ and pixel size 0.03'' we only see a very compact source of flux density 38.0 mJy at 118 MHz (CLEAN beam 0.47'' \times 0.33'' σ = 0.20 mJy/beam), and 42.3 mJy at 154 MHz (CLEAN beam 0.41'' \times 0.25'' σ = 0.11 mJy/beam).

The cumulative corrections derived from J0958 and M81* were then applied to the M82 data. Since M82 is at angular distance 0.6° from M81* residual phase errors might be present in the M82 data limiting the dynamic range, although no clear phase errors are visible in the images. We therefore tried phase-only self-calibration of M82 deriving one solution every five minutes, but this did not result in any significant improvement of the final images. We therefore discarded these corrections, and the images presented in this paper were obtained without any self-calibration on M82. Finally the data were exported from AIPS and converted once more to measurement set (MS) format using the task *exportuvfits* in CASA. To run CLEAN in CASA the MS ANTENNA table had to be manually changed to contain valid “mount type” for all antennas. Since we are not

doing mosaicking, any valid mount type will be treated equally in CASA, and we used mount = “X–Y”.

3. Imaging of M82

Because of the large fractional bandwidth (10%) and large-scale emission present ([Adebahr et al. 2013](#), 5' at λ = 92 cm), deconvolution should be done using multi-scale multi-frequency-synthesis (MSMFS). We deconvolved the calibrated M82 data using the MSMFS algorithm v2.6 as implemented in the task CLEAN in CASA 4.2.1 ([Conway et al. 1990](#); [Rau & Cornwell 2011](#)). A possible dependence of intensity on frequency was taken into account, using the MFS algorithm with two Taylor terms, for all images presented here. Note that no corrections were made for the station beam or other wide-field effects, apart from the corrections applied by *mscorpol*. However, due to the small field of view when imaging, these effects are negligible for all the results presented here, and we did not need to use wide-field imaging software (such as the AW-imager).

3.1. Imaging of compact structure in M82

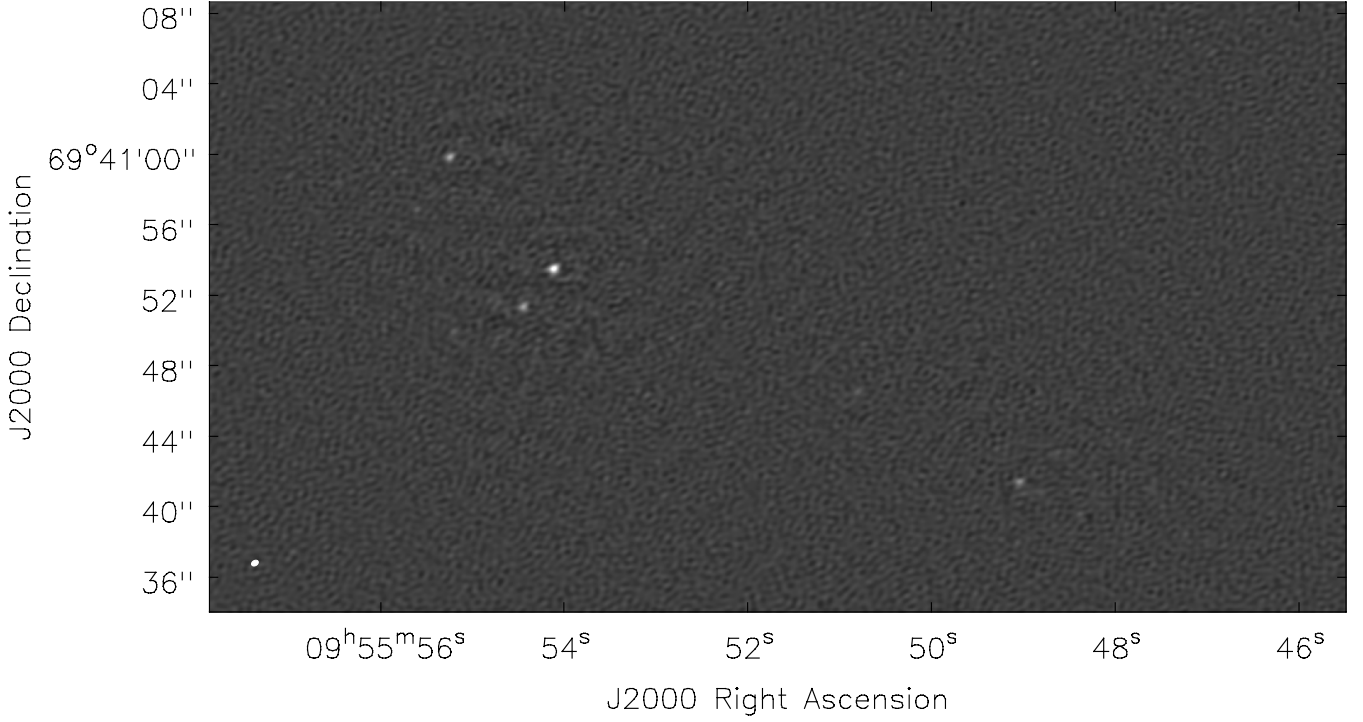
The compact emission was imaged only using baselines longer than 60 k λ and a pixel size of 0.02''. This gave a resolution (CLEAN beam) of 0.45'' \times 0.29'' at 118 MHz and 0.36'' \times 0.23'' at 154 MHz. Since only compact structure was present the multi-scale option was not used here. We found that accounting for a possible intensity gradient with respect to frequency (using MFS with two Taylor terms to model the spectrum of each pixel) produced almost identical results compared to neglecting any spectral gradient (only using one Taylor term). The dirty Stokes *V* images are empty of emission, and from these we estimate the minimum image noise levels as 0.29 mJy/beam at 118 MHz and 0.15 mJy/beam at 154 MHz.

The deconvolved Stokes *I* images, Fig. 2, have rms noise levels of 0.30 mJy/beam at 118 MHz and 0.15 mJy/beam at 154 MHz. The fact that the residuals resemble Gaussian noise, with the same standard deviation in both *I* and *V*, strongly argue that the images are not limited by systematic calibration errors or deconvolution effects. This is not surprising since INT LOFAR, combined with the MFS algorithm, provides excellent sampling of Fourier space in this observation, and because distant interfering sources are decorrelated after averaging visibilities on long baselines in time and frequency. Figure 2b is, to our knowledge, the highest resolution science image ever published at this and lower frequencies. Since the Fourier plane was very well sampled on the smallest scales, the point spread function (PSF) should not introduce imaging artefacts. We think that the minor “artefacts” present in Fig. 2b are in fact due to poorly sampled large scale emission surrounding the compact sources detected. This problem is also experienced when imaging this region of M82 with eMERLIN at higher frequencies.

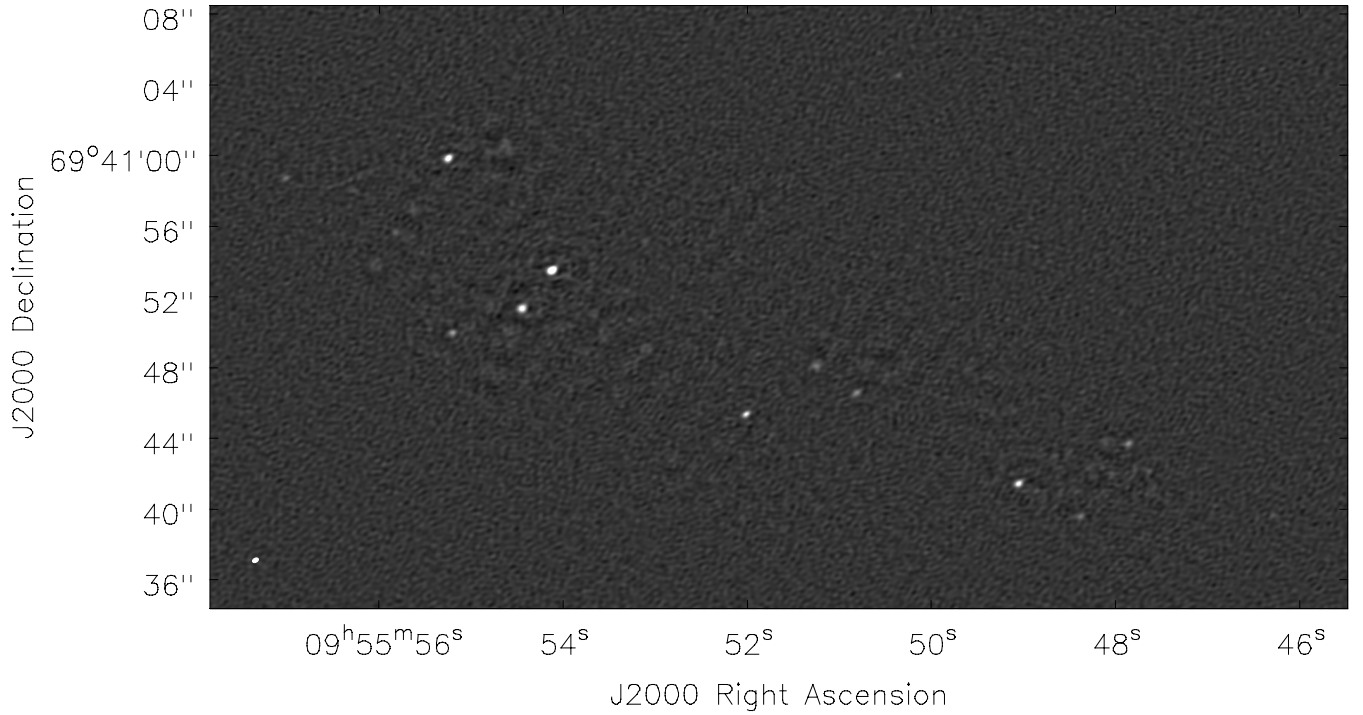
3.1.1. Estimating the thermal image noise

The theoretical image noise for dual polarisation data using natural weighting can be estimated using a modified version (only including international baselines) of the image noise equation given in SKA memo 113 by [Nijboer \(2009\)](#) as

$$\Delta S [\text{Jy/beam}] = W(4\delta\nu\delta t)^{-1/2} \left(\frac{N_{\text{INT}}(N_{\text{INT}} - 1)/2}{S_{\text{INT}}^2} + \frac{N_{\text{INT}}N_{\text{RS}}}{S_{\text{INT}}S_{\text{RS}}} + \frac{N_{\text{INT}}N_{\text{CS}}}{S_{\text{INT}}S_{\text{CS}}} \right)^{-1/2}, \quad (1)$$



(a) Image of M82 at 118 MHz using international (INT) LOFAR baselines.



(b) Image of M82 at 154 MHz using international (INT) LOFAR baselines.

Fig. 2. Images of M82 at 118 MHz (*upper panel*) and 154 MHz (*lower panel*) made using international LOFAR baselines (longer than 60 k λ). The CLEAN restoring beam is shown in the lower left corner of each figure, $0.45'' \times 0.29''$ at 118 MHz and $0.36'' \times 0.23''$ at 154 MHz. The rms noise levels are 0.30 mJy/beam at 118 MHz and 0.15 mJy/beam at 154 MHz. For deconvolution parameters, see Sect. 3.1. Measured brightness values are listed in Table 2.

where W is an extra weighting factor (see below), $\delta\nu$ is the bandwidth [Hz], δt is the integration time [s], N_X is the number of stations of type X , and S_X is the system equivalent flux density (SEFD) of station type X [Jy]. A remote station has been estimated to have a zenith SEFD $S_{RS} \approx 2500$ Jy at 118 MHz and

$S_{RS} \approx 1900$ Jy at 154 MHz (van Haarlem et al. 2013, Fig. 22). In HBA-joined mode we expect a $S_{CS} = S_{RS}$. INT stations are twice as big, hence $S_{INT} \approx 0.5S_{RS}$. In addition, van Haarlem et al. (2013) estimate that the image noise increases by a factor of 1.3 due to time-variable station projection losses, and with a

Table 2. The 16 compact sources detected above 5σ at 154 MHz.

Name	ΔRA [s]	ΔDec [']	$S_{\text{P-118}}$ [mJy/beam]	$S_{\text{I-118}}$ [mJy]	$S_{\text{P-154}}$ [mJy/beam]	$S_{\text{I-154}}$ [mJy]
Uncatalogued	46.300	39.66	–	–	0.76 ± 0.16	0.94 ± 0.26
Uncatalogued	46.415	64.90	–	–	0.74 ± 0.14	0.49 ± 0.27
Uncatalogued	47.644	42.17	–	–	0.85 ± 0.19	1.02 ± 0.30
39.10+57.3 ^{a,b,c,d}	47.869	43.72	–	–	1.94 ± 0.26	2.98 ± 0.40
39.64+53.4 ^{a,b,c,d}	48.389	39.61	–	–	1.42 ± 0.23	2.30 ± 0.36
40.32+55.1 ^{a,b,c,d}	49.060	41.47	3.80 ± 0.51	5.92 ± 0.79	5.17 ± 0.54	6.75 ± 0.73
Uncatalogued	50.366	64.55	–	–	1.05 ± 0.18	1.26 ± 0.27
Uncatalogued	50.820	46.60	1.68 ± 0.36	2.29 ± 0.56	1.92 ± 0.26	3.15 ± 0.41
42.53+61.9 ^a	51.258	48.12	–	–	1.43 ± 0.23	3.72 ± 0.44
43.31+59.2 ^{a,b,c,d}	52.020	45.40	–	–	4.59 ± 0.49	5.01 ± 0.57
45.42+67.4 ^{a,b,c,d}	54.126	53.54	10.88 ± 1.15	17.02 ± 1.91	11.91 ± 1.21	15.98 ± 1.63
45.74+65.2 ^{a,b,c,d}	54.453	51.38	5.13 ± 0.65	8.14 ± 1.01	5.42 ± 0.58	9.05 ± 0.96
46.52+63.9 ^{a,b,c,d}	55.208	49.99	1.70 ± 0.37	1.88 ± 0.60	2.33 ± 0.30	3.08 ± 0.43
46.56+73.8 ^{a,b,c}	55.254	59.87	5.75 ± 0.68	7.97 ± 0.98	6.76 ± 0.70	8.61 ± 0.91
Uncatalogued	55.824	55.68	–	–	1.05 ± 0.20	1.26 ± 0.31
Uncatalogued	57.017	58.75	–	–	1.30 ± 0.20	1.78 ± 0.30

Notes. Four additional possible extended sources are described in Sect. 4.4. Six of the compact sources listed below are detected also at 118 MHz. Fitted peak brightness values are given as S_{P} and integrated flux densities are given as S_{I} . Uncertainties on flux densities were calculated as $((0.1 \cdot \{S_{\text{I}} \text{ or } S_{\text{P}}\})^2 + \sigma_{\text{fit}}^2)^{1/2}$ i.e. including both a 10% calibration uncertainty and the uncertainty estimated from the fit, σ_{fit} . The right ascension and declination are given as offset from 09^h55^m00^s.000 and 69°40′00″.00 (J2000). Sources with names (given traditionally as B1950–offset) were detected previously by ^(a) Wills et al. (1997), ^(b) Fenech et al. (2008), ^(c) Fenech et al. (2010) or ^(d) Gendre et al. (2013). Objects not listed in these studies were marked as “Uncatalogued”. All uncatalogued objects except (46.42, 64.9) were clearly detected also by eMERLIN at 1.6 GHz. See Sect. 4.3 for further notes on source detection.

factor of 1.5 due to the robust weighting used in this paper (as opposed to natural weighting; Briggs 1995). Including these factors as W in Eq. (1) and assuming 16 h integration time, 16 MHz bandwidth, $N_{\text{INT}} = 7$, $N_{\text{RS}} = 13$, and $N_{\text{CS}} = 23$, we estimate our theoretical image noise to be 0.11 mJy/beam at 118 MHz and 0.08 mJy/beam at 154 MHz. It is clear that our measured noise levels are 2.9 times higher than expected at 118 MHz and 1.9 times higher at 154 MHz. This discrepancy is not fully understood, but there are a few noise-increasing factors neglected in the above estimate such as increased station SEFDs when observing at low elevation. The impact of editing should be minor and is in principle possible to calculate, but in practice it is hard for this observation when combining manual and automatic editing procedures and we did not include losses due to editing in the above estimate. Furthermore, the internal calibration of the international stations was not optimal at the time of these observations, thereby increasing S_{INT} . The station calibration has, however, been improved since these data were taken. We note that, despite these hindrances, our attained ratio of image noise to theoretical noise is better than that often attained at lower resolution with LOFAR, where dynamic range constraints can be severe.

3.2. Imaging of extended structure in M82

Before imaging the extended structure using RS–RS and RS–CS baselines, the model obtained through deconvolution of the compact structure (see Sect. 3.1) was subtracted from the data using the task UVSUB in AIPS. The extended emission was then imaged only using baselines of length between 2 and 60 kλ and pixel size 0.4″, giving a resolution (CLEAN beam) of $5.79'' \times 4.53''$ at 118 MHz and $4.65'' \times 3.55''$ at 154 MHz. The multi-scale option was used, and the scales were selected as the geometric series 0, 20, 40, 80, 160 pixels. The largest scale corresponds to the largest scale expected for the core of M82

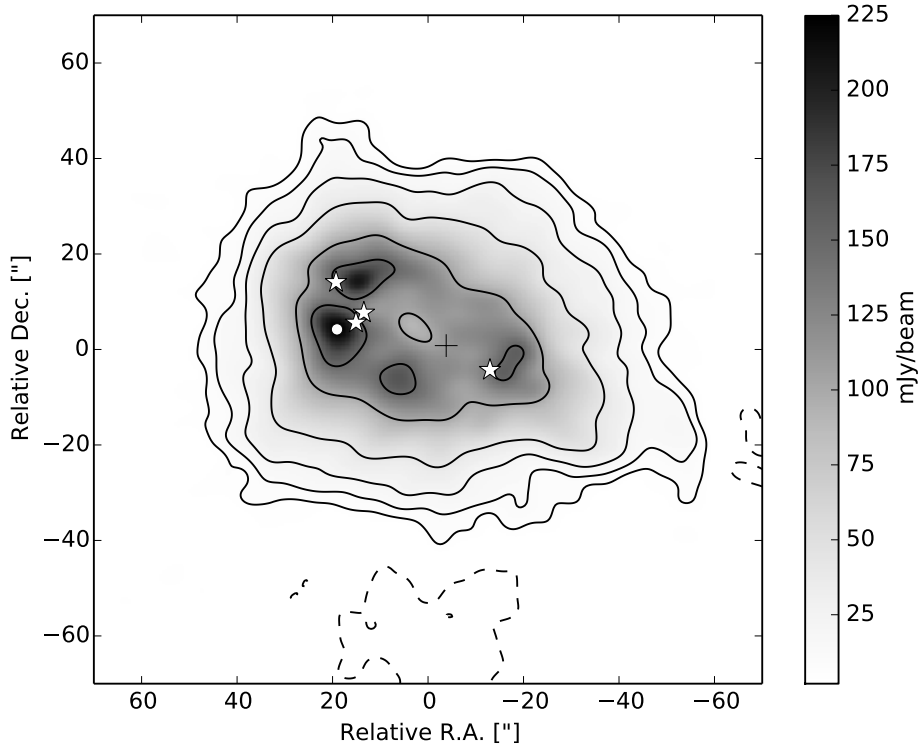
(Adebahr et al. 2013, $\sim 1''$). From imaging of Stokes V , we estimate the minimum image noise to be 0.28 mJy/beam at 118 MHz and 0.15 mJy/beam at 154 MHz. The deconvolved Stokes I images, Fig. 3, have rms noise levels of 0.50 mJy/beam at 118 MHz and 0.27 mJy/beam at 154 MHz, indicating that we either did not successfully deconvolve all the emission present, or there are residual calibration errors limiting the dynamic range.

At RS baselines we are limited by dynamic range rather than random noise. This is not surprising, since at RS baselines the signal from interfering distant cosmic sources is much stronger because of less decorrelation due to averaging. To properly deconvolve such interfering sources, imaging of a larger field of view (possibly with multi-directional calibration) might be needed. Further improvement of the image fidelity by, for example, using different deconvolution algorithms (such as the LOFAR software AW-imager) is however beyond the scope of this work.

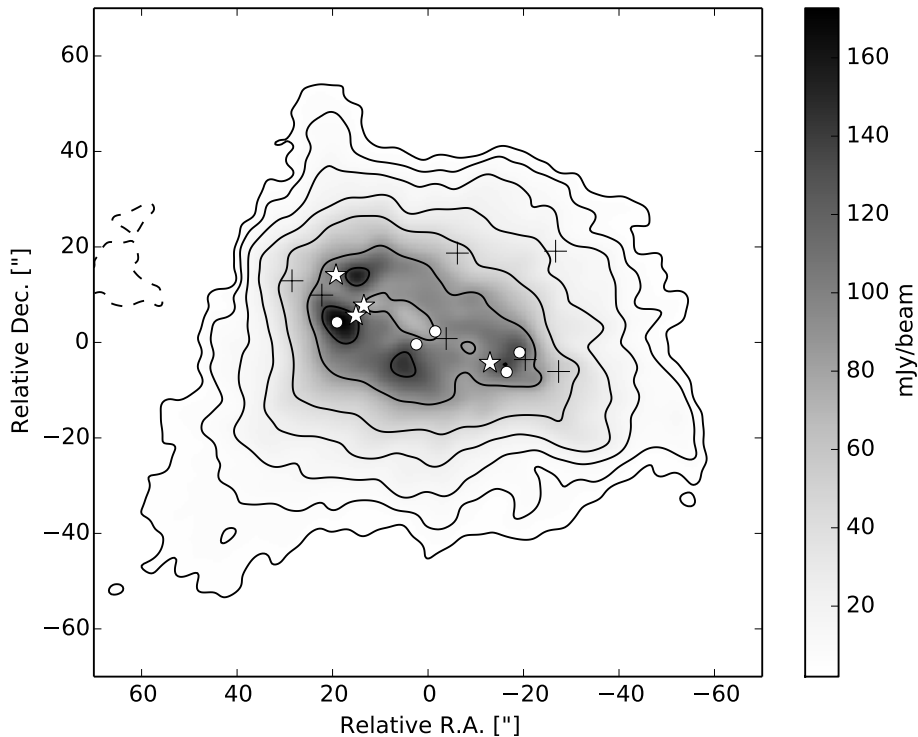
We detect a weak (peak 1.96 mJy/beam) signal in Stokes V at 154 MHz tracing the brightest part of the extended emission visible in Fig. 3b. This signal could be real, but could also be a residual polarisation error. In particular, the conversion to circular polarisation introduces a good, but approximate, parallactic angle correction. This, plus possible gain differences and/or phase offsets between X and Y, may cause leakage between the derived R and L. A complete polarisation calibration is beyond the scope of this work, and will only marginally affect the Stokes I measurements presented here.

3.3. Summary of calibration and imaging

For convenience, let us summarise the calibration and imaging procedures described in the previous sections. The observing mode used in this paper made use of a primary calibrator, J0958, 4 degrees distant from M82 to determine delays and rates and initial phase solutions. These delay, rate and phase solutions



(a) Image of M82 at 118 MHz using remote (RS) LOFAR baselines.



(b) Image of M82 at 154 MHz using remote (RS) LOFAR baselines.

Fig. 3. Images of M82 at 118 MHz (*upper panel*) and 154 MHz (*lower panel*) made using LOFAR baselines of length between $2\text{ k}\lambda$ and $60\text{ k}\lambda$ (robust 0 weighting). At 118 MHz the synthesised PSF (beam) is $5.79'' \times 4.53''$ and the rms noise is $\sigma_{118} = 0.50\text{ mJy/beam}$. At 154 MHz the PSF is $4.66'' \times 3.56''$ and the rms noise is $\sigma_{154} = 0.27\text{ mJy/beam}$. For deconvolution parameters, see Sect. 3.2. These images show the structure of the extended emission in grey scale (with brightness per respective beam size). The upper panel contours are drawn at $(-10, 10, 20, 40, 80, 200, 300) \times \sigma_{118}$ and the lower panel contours are $(-10, 10, 20, 40, 80, 160, 320, 500) \times \sigma_{154}$. The symbols mark the positions of the sources listed in Table 2. The stars mark the power law-spectrum objects, shown in Fig. 5. The circles mark the turnover-spectrum objects, shown in Fig. 6. The plus signs mark the remaining objects listed in Table 2. Positions are given relative to the M82 position in Table 1.

were then transferred (3.5°) to M81* which then allowed, by averaging over longer timescales and frequency ranges, phase-only self-calibration solutions to be determined toward the much weaker (40 mJy) M81* nucleus. The amplitude scale was set by the observed flux density of 3C 196. Transferring these phase solutions 0.6° to M82 allowed random noise limited images to be made.

4. Results and discussion

In this section we present the results along with a brief discussion of the properties of the compact and diffuse emission seen in Figs. 2 and 3. Fitted quantities for all compact features detected in Fig. 2 are summarised in Table 2. The fitting was done using the software PyBDSM v1.8.2 with default parameters except but

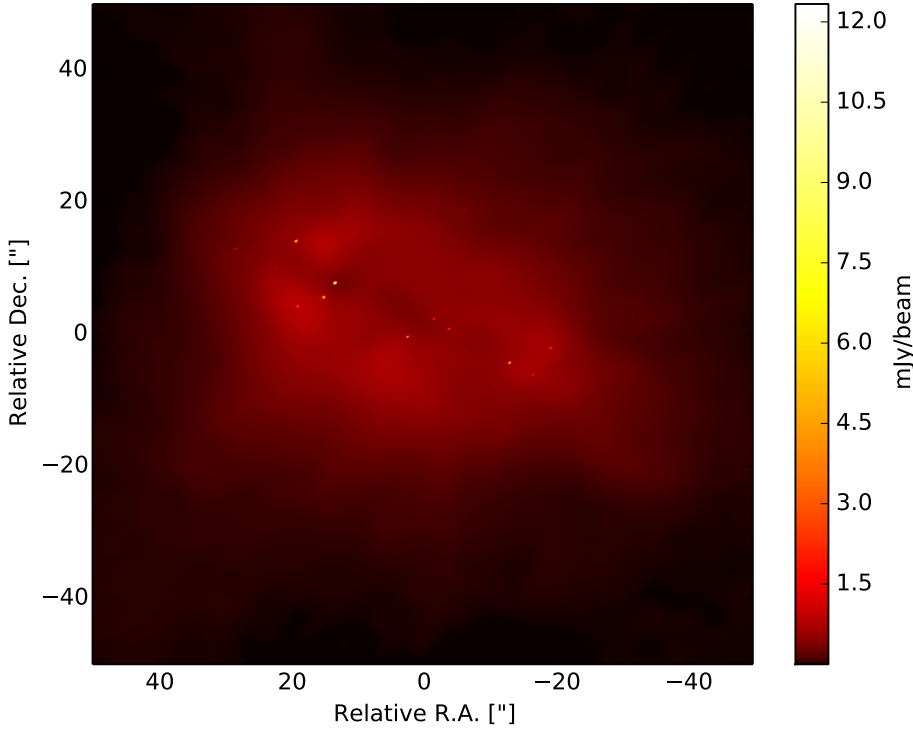


Fig. 4. Combined image illustrating the relative brightness between the compact and extended emission at 154 MHz. This image was made by combining (using the task *feather* in CASA) the RS image (Fig. 3b) with a thresholded version of the INT image, Fig. 2b, only including emission brighter than 4σ . The threshold was needed to remove the relatively strong noise in the INT image which would otherwise distort the weaker parts of the extended emission. Since the brightness difference between compact and extended emission is large, a square-root colour scale is used to better show the large scale emission. The colour scale is in mJy/beam, where the beam is the INT beam in Fig. 2b, i.e., $0.36'' \times 0.23''$. Positions are given relative to the M82 position in Table 1.

specifying “hard” clipping at peak level of 5σ and island level of 3σ .

4.1. Positional accuracy

Based on the dynamic range in the images we estimate an average positional uncertainty of $0.04''$ for the objects listed in Table 2. When matching source positions with literature we allowed for an extra $0.05''$ difference since most MERLIN positions were rounded to $0.1''$ in Dec. We note that the LOFAR positions appear approximately 60 mas south-west of the eMERLIN 1.6 GHz positions. This offset is visible in Figs. 7a and c, but is also present for the brighter objects. We believe that this offset is not due to spectral shifts in any particular object in M82. In this paper the M82 positions are phase-referenced to M81* assuming the position for M81* given in Table 1. Because of the 0.6° angular separation between M81* and M82, position errors may be introduced by slowly varying (i.e. few hours, otherwise averaged when imaging) differences in ionospheric refraction in the two directions. Again using the simple slab approximation for the ionosphere, as in Sect. 2.2.4, we can roughly estimate the residual delay as 1 ns over 0.6° , corresponding to a position offset of 60 mas for a 1000 km baseline.

In addition to possible ionospheric shifts, we note that M81* is known to have a core shift at GHz frequencies; the peak of emission is shifted to the north-east at lower frequencies with respect to images at higher frequencies (Bietenholz et al. 2004; Martí-Vidal et al. 2011b), i.e. consistent with the offset seen between LOFAR and eMERLIN. Assuming that the power laws, describing the decrease in the particle density and/or magnetic field as a function of distance to the jet base, do not change over the whole jet, we estimate, using the jet model presented by Martí-Vidal et al. (2011b), the offset due to the core-shift in M81* to be 10 mas between 150 MHz and 1.6 GHz. In conclusion, we find that the offset may be explained by either the ionosphere, or a core-shift in M81*, or a combination of both.

4.2. The shape and flux of the diffuse emission

The diffuse emission, Fig. 3, shows a “ring”-like structure with a “hole” in the centre. The “ring” we interpret as coming from emission above and below the starburst disk at the base of the large scale outflow, perhaps more clearly visible in the combined INT+RS colour image, see Fig. 4. The minimum brightness in the hole is less than half the peak brightness of the surrounding ring. In addition to the central hole, we see a decrease in extended emission tracing the region where most of the compact objects listed in Table 2 are located. We interpret this decrease as due to free-free absorption by the central star forming disk, seen almost edge-on.

Integrated flux densities were obtained by summing pixels above 2σ clearly associated with M82 in Fig. 3. At 118 MHz we obtain 12.0 ± 1.2 Jy with a peak of 225 mJy/beam, and at 154 MHz we obtain 13.5 ± 1.4 Jy with peak of 173 mJy/beam. The middle hole has a minimum brightness of 91 mJy/beam at 118 MHz and 70 mJy/beam at 154 MHz. Although absorption has a clear impact on some parts of the core, the integrated flux densities measured at 118 and 154 MHz show that the central parts of M82 are brighter than the ~ 5 Jy expected based on detailed modelling of M82 (Lacki 2013, Fig. 5).

When imaging Fig. 3 we excluded baselines shorter than $2\text{ k}\lambda$, hence we miss flux present at the largest spatial scales. It follows that the flux densities recovered here for the extended emission are to be regarded as lower limits at the respective frequencies. Images of M82 also including shorter baselines will be published in a forthcoming paper.

4.3. The “uncatalogued” compact objects

In Table 2 we label some compact objects, seen in Fig. 2, as “uncatalogued”. Most sources seen with LOFAR are almost certainly old SNRs, some of which have either not been detected previously due to insufficient sensitivity, or have not been

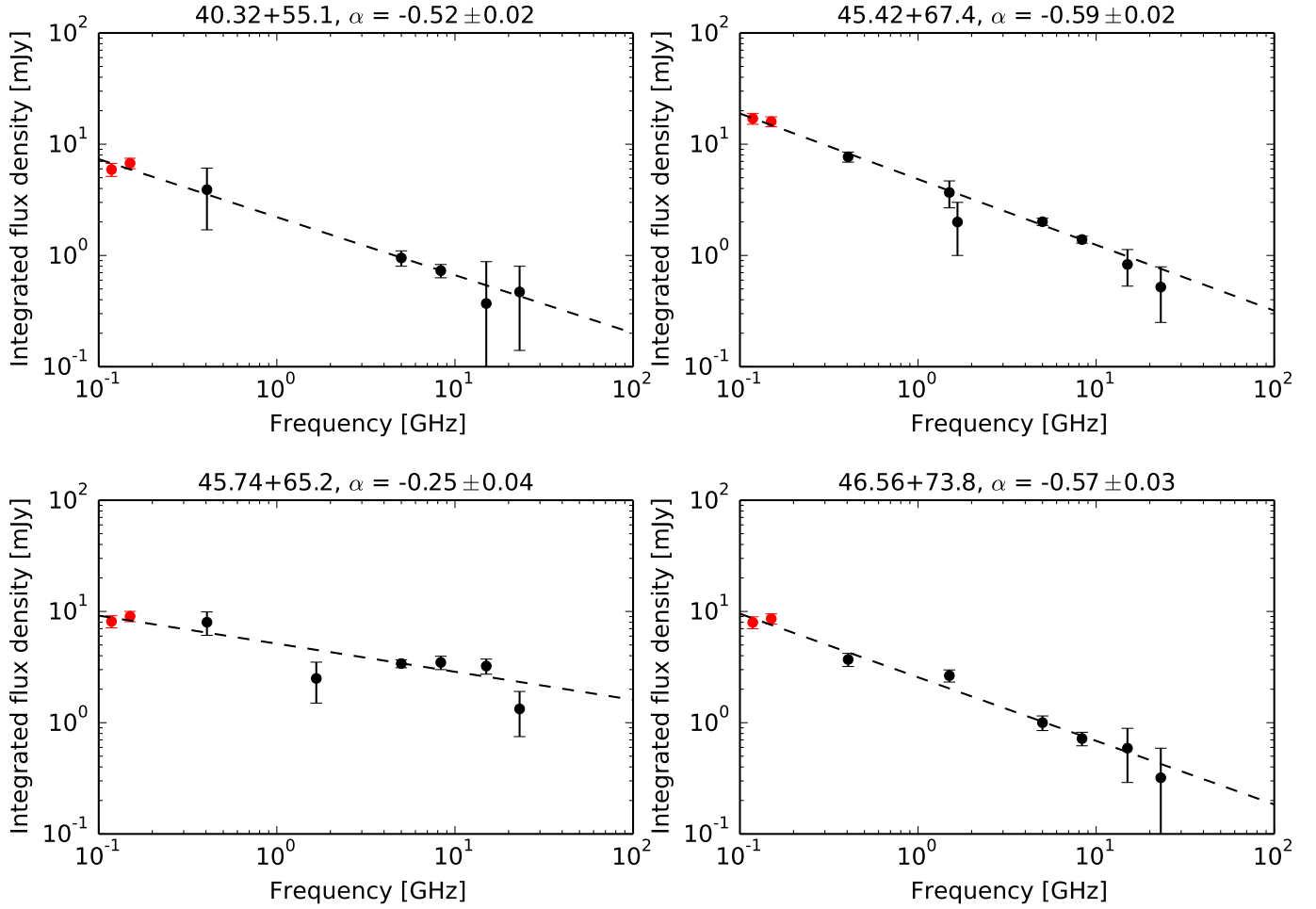


Fig. 5. Spectra of four compact objects detected with LOFAR, and also reported at 408 MHz by Wills et al. (1997). These objects show no low-frequency turn-over at LOFAR frequencies. LOFAR data points are plotted in red. Non-LOFAR data points are VLA and MERLIN, as presented in Table 2 by Allen & Kronberg (1998). A simple power law ($S_\nu \propto \nu^\alpha$) was fitted and is plotted as a dashed line. The best fit α is given in the respective figure title.

reported because of selection effects. Previous studies have used different selection criteria for when to report a detection. For example, Wills et al. (1997) reported sources detected at 408 MHz only if they were brighter than 1 mJy at 5 GHz. In fact, a preliminary re-analysis of the original Wills 408 MHz data show evidence of emission from three objects reported as “uncatalogued” in Table 2: (50.820, 46.60; 2.1 mJy), (55.824, 55.68; 1.2 mJy), and (57.017, 58.75; 1.8 mJy). We note, by visual inspection of the recent 1.6 GHz eMERLIN observations, that all but one (at position 46.42, 64.9 in Table 2) of the uncatalogued objects detected with LOFAR at 154 MHz are also present at 1.6 GHz. This strongly suggests that these objects are real.

4.4. Do we detect HII regions?

To calculate a lower limit on the brightness temperatures of the detected sources we can use Eq. (5) by Condon et al. (1991): $T_b = (c^2 S_\nu / 2k\nu^2) \times (8\ln(2)/3\pi\theta_M\theta_m)$. Assuming a uniform elliptical source component with angular diameters $\theta_M = 0.36''$, $\theta_m = 0.23''$ (beam size), and integrated flux density 5×0.15 mJy (detection threshold), we find a lower limit of $10^{5.5}$ K for the compact sources detected at 154 MHz. Thermal (free-free) emission from ionised gas in HII regions have brightness temperatures up to 2×10^4 K (Wilson et al. 2009, Sect. 11.2.1). The high

resolution of our image thus allows us to discard the hypothesis that the objects listed in Table 2 are simple HII regions.

4.5. Low-frequency spectra of compact objects

Our observations provide important constraints on the (likely) foreground free-free absorption due to ionised gas, not only of the detected objects in Table 2, but also as upper limits on all sources seen at higher frequencies but not detected here. To illustrate this we chose the five brightest objects at 1.7 GHz listed by Fenech et al. (2010): 41.95+57.5 (38.25 mJy), 43.31+59.2 (23.55 mJy), 45.17+61.2 (17.60 mJy), 44.01+59.6 (12.32 mJy), and 40.68+55.1 (11.33 mJy). Of these, only 43.31+59.2 is detected at 154 MHz (5 mJy). We note in particular that the brightest object at 1.7 GHz, 41.95+57.5, was measured to be 100 mJy at 408 MHz by Wills et al. (1997) but we do not detect any emission with LOFAR at this position. The spectrum of this source is, however, known to evolve over time and significant changes are expected during the two decades since the 408 MHz data were taken. Based on 4.8 GHz observations, Allen & Kronberg (1998) derive a decay rate of $8.8\% \text{ yr}^{-1}$ for this object, but the decay estimate is uncertain for lower frequencies. Future modelling of this object may use these LOFAR measurements to better constrain the spectral evolution also at low frequencies.

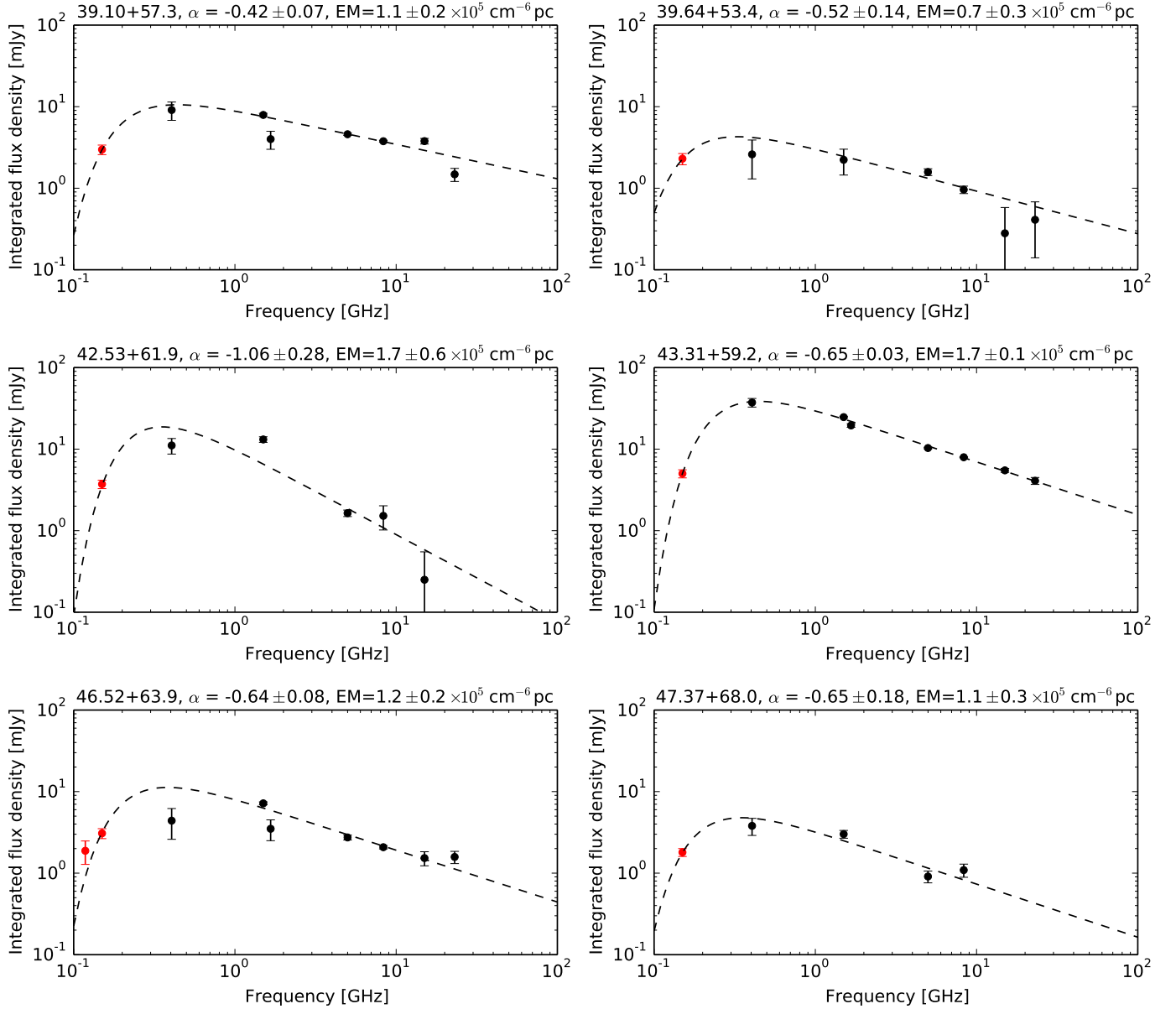


Fig. 6. Spectra of six objects detected with LOFAR, and also reported at 408 MHz by Wills et al. (1997). Five of these are compact and listed in Table 2, while “47.37+68.0” is resolved and discussed in Sect. 4.6. These objects show evidence of a low-frequency turn-over at LOFAR frequencies. LOFAR data points are plotted in red. Non-LOFAR data points are VLA and MERLIN, as presented in Table 2 by Allen & Kronberg (1998). A model of SNR spectra was fitted to each object as described in Sect. 4.5. The best fit spectral index α and emission measure EM are given in the respective figure title.

4.5.1. Sources detected also at 408 MHz

To connect these results to the previous subarcsecond images of M82 at 408 MHz, we selected the nine sources listed in Table 2 where 408 MHz flux densities were reported by Wills et al. (1997). We find that the spectra of four objects can be fitted by a power law (see Fig. 5) i.e., no evidence of spectral turnovers down to 118 MHz. Three of these sources have spectral indices typical of SNRs or young supernovae ($\alpha \approx -0.5$) but one object (45.74+65.2) has a flatter spectrum ($\alpha \approx -0.3$); these objects are discussed in Sect. 4.5.2.

The remaining five sources show indications of a low-frequency turnover, see Fig. 6. We have attempted to fit the spectra of these sources using the model used by Wills et al. (1997). In this model, the emission comes from a background source

(i.e. the SNR) with spectral index α and is attenuated by foreground free-free absorption. The spectrum S_ν is described as $S_\nu \propto \nu^\alpha e^{-\tau}$, where $\tau = 8.2 \times 10^{-2} \nu^{-2.1} \text{EM}/T_e^{1.35}$ and EM is the emission measure in $\text{cm}^{-6} \text{pc}$, ν the frequency in GHz and T_e is the electron temperature, taken to be 10 000 K. A more detailed analysis based on fitting also upper limits for many more sources will be presented in a forthcoming paper.

The best fitting model was found using standard least-squared fitting in SciPy and the best fit parameters α and EM are given in the respective figure title. For these objects LOFAR provides a very important addition to the spectrum and makes it possible to determine the emission measure with higher precision than before. We note that the fitted EM values are in the relatively narrow range $0.7\text{--}1.7 \times 10^5 \text{ cm}^{-6} \text{pc}$, but given the small number statistics we refrain from further analysis of

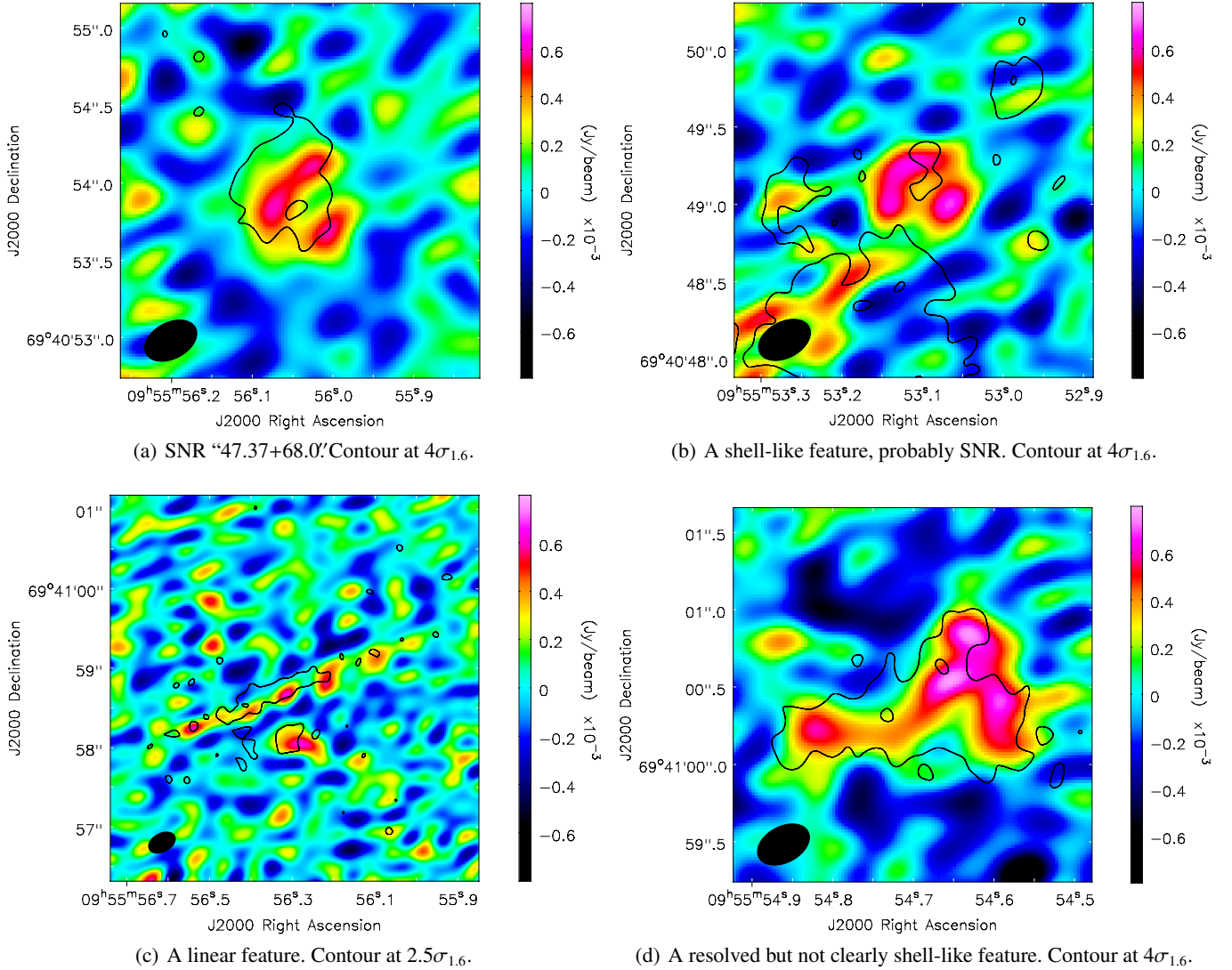


Fig. 7. Zoom on four weak but resolved features seen in Fig. 2b. The LOFAR 154 MHz-beam is shown in the lower left corner. Each feature is briefly discussed in Sect. 4.6 where flux densities and positions are given. Colours are LOFAR 154 MHz, contours are eMERLIN at 1.6 GHz ($\sigma_{1.6} = 16 \mu\text{Jy}/\text{beam}$, Pérez-Torres et al. 2014), see respective panel text for contour levels. The *top* panels show two shell-like structures; the *top-left* is identified as the SNR listed as “47.37+68.0” by Wills et al. (1997), while the *top-right* is uncatalogued. The *bottom-left* panel shows a linear feature and *bottom-right* shows a resolved but not clearly shell-like object. Note that the bottom-left panel covers a larger area on sky, and has lower contour levels, compared to the other three panels. We note a minor positional offset of approximately 60 mas between the LOFAR and eMERLIN images, see Sect. 4.1 for a brief discussion on positional accuracy.

the EM range. We note that detailed models of SNR evolution may differentiate between internal and external free-free absorption mechanisms, see for example DeLaney et al. (2014) for Cassiopeia A. Unfortunately we do not yet have enough measurements of the sources in M82 to properly separate these effects.

With bright SNRs it is also possible to study the cold, diffuse ISM through absorption as radio recombination lines (RRLs). This was recently done in M82 using LOFAR LBA by Morabito et al. (2014) although this detection only used the shortest LOFAR baselines and hence could not spatially resolve and locate the RRLs within M82. In a future publication we aim to map the RRLs detected by Morabito et al. (2014) by using the techniques explained in this paper for calibration and imaging of international and remote baselines, as well as search for and map RRLs within the HBA data presented here.

4.5.2. Flattening of spectra

In the objects 42.35+61.9 and 46.52+63.9 the model does not represent the data very well. The measured spectra of these objects are flatter and the turn-over frequency higher than the best-fit model. A flattening of the spectrum (as also seen in 45.74+65.2) can be explained by ejecta-opacity effects in the shell of a radio SNR, as observed in SN1993J by Martí-Vidal et al. (2011a). In this case, the ejecta becomes optically thin at higher frequencies and allow us to see emission also from the rear side of the shell at higher frequencies, hence flattening the spectrum. The source with the flattest spectrum, 45.74+65.2, is clearly a SNR as seen in Fenech et al. (2010), their Fig. 3, and since it is bright (third brightest at 154 MHz) ejecta-opacity effects could be important. Another possible explanation is that this object is a plerion-shell composite, see e.g.

Weiler & Sramek (1988). More advanced modelling of these spectra will be presented in a future paper.

4.5.3. The eMERLIN transient 43.78+59.3

A “transient” source was reported by Muxlow et al. (2010) at position $09^{\text{h}}55^{\text{m}}52^{\text{s}}.5083$ and $69^{\circ}40'45''.410$ (J2000). At 118 MHz we do not detect anything at this position. At 154 MHz we find a weak (0.45 mJy/beam) signal at position $09^{\text{h}}55^{\text{m}}52^{\text{s}}.520$, $69^{\circ}40'45''.43$ (J2000). This may be associated with 43.78+59.3 but since it is so weak (only 3σ) we do not claim a detection and treat this as an upper limit.

4.5.4. No detection of SN2008iz

SN2008iz (Brunthaler et al. 2009) is not detected in these observations; the maximum value which could be associated with this source is 0.90 mJy/beam at 118 MHz and 0.41 mJy/beam at 154 MHz, i.e. $<3\sigma$. This source was originally predicted to be 140 mJy at 154 MHz (at the time of this observation), using the standard mini-shell model for radio SNe (Chevalier 1982a,b; Weiler et al. 2002). However, recent elaborate multi-frequency modelling using all available data for this object, and adding a low-frequency cutoff due to the Razin-Tsytovich effect (the suppression of the emission below a certain frequency due to plasma propagation effects), predict a flux density at 154 MHz of 10^{-4} mJy at the time of these observations (Martí-Vidal et al., in prep.), i.e. well below our detection limit.

4.6. Four weak resolved objects

In addition to the compact objects listed in Table 2 we find four resolved features in Fig. 2b which, although weaker than our point source sensitivity of 5σ , are above several sigma over multiple beams and/or correspond to structure seen at higher frequencies and which we are confident are real. Cutouts of each of these features are shown in Figs. 7a to d.

4.6.1. Two weak shell-like features

Two weak shell-like features, with diameters $\sim 0.4''$, are seen at 154 MHz, see top panels in Fig. 7.

One (top-left panel) has central position at $09^{\text{h}}55^{\text{m}}56^{\text{s}}.030$, $69^{\circ}40'53''.80$ (J2000) with peak flux density 0.6 mJy/beam and integrated flux density 1.8 mJy/beam (summing by eye pixels associated with the source). We identify this object as the source “47.37+ 68.0” as listed by Wills et al. (1997). This object was not included in Table 2 since the peak is formally below our detection threshold. However, given the clear shell-like structure, the significant integrated flux density, and the good match with previous observations, we include this source in the spectral fits presented in Fig. 6, with a flux density of 1.8 ± 0.2 mJy at 154 MHz. The fitted spectrum indicates a low-frequency turnover below 408 MHz, see bottom-right panel in Fig. 6.

The second shell-like feature (top-right panel) has centre position at $09^{\text{h}}55^{\text{m}}53^{\text{s}}.100$, $69^{\circ}40'49''.10$ (J2000) with peak brightness of 0.7 mJy/beam and integrated flux density 1.8 mJy at 154 MHz, and a peak of 0.1 mJy/beam and integrated flux density of 0.3 mJy at 1.6 GHz. It is hard to accurately measure the integrated flux density at 1.6 GHz for this object because of nearby large-scale emission sampled with eMERLIN at this frequency. This object is very similar in structure and flux density at

154 MHz to “47.37+68.0”, but we could not find a corresponding source catalogued in either of Wills et al. (1997), Fenech et al. (2008, 2010), or Gendre et al. (2013). This object is probably an SNR which, because of the nearby confusing large-scale emission, has not previously been clearly identified.

4.6.2. A peculiar linear feature

In the north-east part of the Fig. 2b we see a linear feature (zoom in Fig. 7c) extending $3''$ (50 pc) i.e. for 10 beams, not aligned with the disk of M82. This object has an integrated flux density of 2.1 mJy and a peak of 0.6 mJy/beam (only seen at 154 MHz). Although formally below our detection limit, this object was also detected in recent eMERLIN observations at 1.6 GHz, see Fig. 7c, with an integrated flux density of 1.5 mJy. This feature is similar in size (50 pc) to the non-thermal radio filaments seen prominently in the direction perpendicular to the Galactic plane² (Yusef-Zadeh & Morris 1987). However, these radio filaments were observed by Law et al. (2008) to have flux densities of ~ 20 – 200 mJy at 20 cm wavelength which, given the distance ratio of ~ 400 would appear as $\sim 1 \mu\text{Jy}$ in M82. The observed flux density at 1.6 GHz is more than a thousand times the luminosity expected if this was a non-thermal filament similar to those in the centre of the Milky way. We refrain from further speculation about the nature of this source.

4.6.3. A resolved but not clearly shell-like object

At position $09^{\text{h}}55^{\text{m}}54^{\text{s}}.62$ and $69^{\circ}41'00''.5$ (J2000) is a clearly resolved object (see zoom in Fig. 7d) with peak flux density 0.8 mJy/beam and integrated flux density 4.5 mJy at 154 MHz. With chosen input parameters, PyBDSM did not detect it (parameters given in Sect. 4), but it is clearly seen also in recent eMERLIN 1.6 GHz observations where an integrated flux density of 5.5 mJy and a peak brightness of $140 \mu\text{Jy/beam}$ (eMERLIN beam $150'' \times 126''$) is recovered for this source. This object was not seen by either of Wills et al. (1997), Fenech et al. (2008, 2010), Gendre et al. (2013). However, as discussed in Sect. 4.3, this resolved object is probably old but since it is faint it might not have been detectable without the now improved sensitivity of eMERLIN.

4.7. Implications for LOFAR international baseline Imaging

The results presented in this paper show that sensitive ($\sigma = 0.15$ mJy/beam) random noise-limited images of complex sources can be made at HBA frequencies with international LOFAR baselines. The images obtained set a new record in terms of combined resolution and sensitivity for science images at frequencies below 327 MHz. These data were reduced in a relatively straightforward manner using conventional VLBI imaging techniques. LOFAR international baseline imaging, although often perceived as more difficult than imaging on Dutch baselines, can in fact be less computationally expensive and algorithmically complex. International baseline imaging is in many aspects simpler than Dutch baseline imaging, because we can generally ignore interference from other bright sources in the sky. The effect of one source on the position of another is greatly reduced by time and frequency coherence losses such that each compact source can be imaged independently in small fields.

For a distant potentially interfering source, the interfering contribution to the target source visibility declines by factors of

² See also <http://apod.nasa.gov/apod/ap080427.html>

u^{-1} as a function of baseline length (u) for both frequency and time decorrelation. Furthermore, for most of the source population resolved on longer Dutch LOFAR baselines, the intrinsic visibility structure decreases faster than u^{-2} (a rough approximation based on experience of typical dependence of visibility amplitude vs. baseline length for resolved radio sources), giving a total decrease of interfering signals with baseline length scaling as u^{-4} . This means that the effect of interfering signals is a million times less for baselines of 1000 km as opposed to 30 km. This effect explains why the influence of the brightest sources at LOFAR frequencies, like Cassiopeia A or Cygnus A, can be ignored at international baseline resolution, as can most Jansky level sources within the station beam.

The small field of view regime is where cm-VLBI usually operates and this regime greatly simplifies imaging. In this regime, target images are generally smaller than the isoplanatic patch, and therefore only a single-direction station-dependent correction needs to be determined. Likewise, over such small fields, w -term effects and station beam variations can generally be ignored. This is different from LOFAR core-resolution imaging, where in order to get noise-limited (rather than “dynamic range”-limited) images at any given point in a field the whole field must be imaged using multi-directional calibration techniques. In the intermediate regime of LOFAR Dutch remote (<100 km) baselines we have shown that on a very bright target source such as M82 it is also possible to get useful science images by standard VLBI techniques, as demonstrated by Fig. 3b. Further increasing the image sensitivity by deconvolving interfering sources may require other techniques.

Whether one can produce useful images using the small-field approximation and VLBI software depends on the brightness of the target source and, if necessary, the availability of close sources to use as calibrators similar to what is done in cm-VLBI. A new pipeline is being developed by Moldón et al. (2015) to help quickly identify nearer calibrators, which should make the calibration process more robust by reducing the degree of spatial extrapolation.

4.8. Future data analysis and observations

This paper has concentrated on presenting the imaging results applying VLBI techniques to the analysis of international and Dutch remote baselines. We have shown that these techniques can be used to obtain high dynamic range images close to the thermal noise. Based on Fig. 3b the positions of SNRs showing low-frequency turnovers and SNRs not showing a turnover are distributed randomly with respect to stronger and weaker absorption features in the diffuse emission. This suggests that the free-free absorbing ionised medium is clumpy rather than uniform, as discussed by Lacki (2013). However, this can be better constrained by also modelling the spectrum of the diffuse emission. A subsequent analysis paper will jointly model the spectra of the compact sources and the diffuse emission in which they are embedded. Other data sets on M82 have been observed, optimised to image the extended halo structure at HBA and LBA frequencies and will be presented elsewhere (Adebahr et al., in prep.). This paper only presents results on M82, the M81* data is yet to be fully analysed and we will attempt in future work to characterise the low-frequency structure of the M81 nucleus, detect or set limits on the flux density of SN1993J, and try to detect other SNRs in M81.

It is clear from the observations presented here that there are many compact objects in M82 at, or just below, our sensitivity detection level. Modest improvements in sensitivity, achievable

in follow-up observations, will allow us to detect more sources. It should be noted that the observational setup used for the observations presented in this paper was designed in order to minimise the data processing needed rather than to maximise sensitivity. In particular, the bandwidth was split equally three ways between M82, M81* and the bright calibrator, and each was allocated a separate station beam. The sources M81* and M82 are close enough that they are well within the same station beam, and can in subsequent observations be observed simultaneously within one beam at full bandwidth. In addition to this, we can use the procedure suggested by Moldón et al. (2015) to identify a closer primary calibrator for M82, which can also be observed in the same beam. To use this “three source in one beam”-technique we need to store initially the data after correlation with high temporal and spectral resolution, phase rotate the data to the position of the two sources, and average in time and frequency. This is conceptually simple but requires processing large volumes of (temporary) data. Efforts are underway to implement and automate such a pipeline (Moldón et al. 2015). As a practical matter such processing should therefore be done immediately after correlation on the correlator output cluster, before shipping data to other facilities.

The results in this paper show that the prospects for science exploitation of LOFAR international baseline data are excellent and the data analysis in principle straightforward. To make it more exploitable by the general community, software for non-experts is being implemented. A significant issue that has to date limited the exploitation of LOFAR international baselines has been the reliability of the data links between the international stations and the correlator (the international stations themselves show high reliability) but recently much progress has been made in solving this issue. For optimal sensitivity and speed in the calibration process it is also desirable to use more general full-bandwidth fringe-fitting strategies that fully include non-dispersive and dispersive delays as well as differential Faraday rotation. Software to enable such calibration techniques is currently under development.

5. Summary

The International LOFAR telescope has been used to make subarcsecond resolution images of the sky at 118 MHz and 154 MHz. Our 154 MHz continuum image using international baselines, with a synthesised beam of $0.36'' \times 0.23''$ and rms noise 0.15 mJy/beam, is a new record in terms of combined image resolution and point-source sensitivity for science images at frequencies below 327 MHz.

In our high-resolution image, we detect 16 compact objects above 5σ at 154 MHz within the inner $1'$ of M82. Six of these are also detected above 5σ at 118 MHz. Four resolved features are seen (but with peak flux densities below 5σ) in the high-resolution image. These are also seen with eMERLIN at 1.6 GHz.

In contrast to predictions of the standard RSNe model (Chevalier 1982a,b; Weiler et al. 2002), we do not detect any emission ($<3\sigma$) from supernova 2008iz. However, new modelling, accounting for significant plasma effects in the shocked region, is in good agreement with our observations. We do not detect ($<3\sigma$) the eMERLIN transient source 43.78+59.3, nor the object 41.95+57.5 which is the brightest compact object at 1.7 GHz. Using data on Dutch (remote) baselines, we find diffuse emission surrounding compact objects with total integrated flux density 12.0 ± 1.2 Jy at 118 MHz and 13.5 ± 1.4 Jy at 154 MHz. Significant absorption is seen along the star forming disk where

most of the compact objects are located. The strongest absorption is seen towards the centre of M82 as a “hole” in the diffuse emission.

Further analysis, also using upper limits imposed by these observations on sources not detected here, will make it possible to trace the spatial structure (uniform/clumpy) of the absorbing ionised gas component present in the nucleus of M82.

Acknowledgements. We acknowledge assistance by the LOFAR science support as well as Simon Casey for installing LOFAR software in Onsala. This research has made use of the NASA/IPAC Extragalactic Database (NED) which is operated by the Jet Propulsion Laboratory, California Institute of Technology, under contract with the National Aeronautics and Space Administration. The research leading to these results has received funding from the European Commission Seventh Framework Programme (FP/2007–2013) under grant agreement No. 283393 (RadioNet3). e-MERLIN is the UK’s National Radio Interferometric facility, operated by the University of Manchester on behalf of the Science and Technology Facilities Council (STFC). LOFAR, the Low Frequency Array, designed and constructed by ASTRON, has facilities in several countries, that are owned by various parties (each with their own funding sources), and that are collectively operated by the International LOFAR Telescope (ILT) foundation under a joint scientific policy.

References

- Adebahr, B., Krause, M., Klein, U., et al. 2013, *A&A*, 555, A23
- Allen, M. L., & Kronberg, P. P. 1998, *ApJ*, 502, 218
- Ananthakrishnan, S., Kulkarni, V. K., Ponsonby, J. E. B., et al. 1989, *MNRAS*, 237, 341
- Bietenholz, M. F., Bartel, N., & Rupen, M. P. 2004, *ApJ*, 615, 173
- Briggs, D. S. 1995, Ph.D. Thesis, The New Mexico Institute of Mining and Technology
- Brunthaler, A., Menten, K. M., Reid, M. J., et al. 2009, *A&A*, 499, L17
- Carr, T. D., Lynch, M. A., Paul, M. P., et al. 1970, *Radio Sci.*, 5, 1223
- Chevalier, R. A. 1982a, *ApJ*, 258, 790
- Chevalier, R. A. 1982b, *ApJ*, 259, 302
- Clark, T. A., Erickson, W. C., Hutton, L. K., et al. 1975, *AJ*, 80, 923
- Cohen, A. S., Lane, W. M., Cotton, W. D., et al. 2007, *AJ*, 134, 1245
- Condon, J. J. 1992, *ARA&A*, 30, 575
- Condon, J. J., Huang, Z.-P., Yin, Q. F., & Thuan, T. X. 1991, *ApJ*, 378, 65
- Conway, J. E., Cornwell, T. J., & Wilkinson, P. N. 1990, *MNRAS*, 246, 490
- DeLaney, T., Kassim, N. E., Rudnick, L., & Perley, R. A. 2014, *ApJ*, 785, 7
- Fenech, D. M., Muxlow, T. W. B., Beswick, R. J., Pedlar, A., & Argo, M. K. 2008, *MNRAS*, 391, 1384
- Fenech, D., Beswick, R., Muxlow, T. W. B., Pedlar, A., & Argo, M. K. 2010, *MNRAS*, 408, 607
- Gendre, M. A., Fenech, D. M., Beswick, R. J., Muxlow, T. W. B., & Argo, M. K. 2013, *MNRAS*, 431, 1107
- Greisen, E. W. 2003, *Information Handling in Astronomy – Historical Vistas*, 285, 109
- Israel, F. P., & Mahoney, M. J. 1990, *ApJ*, 352, 30
- Israel, F. P., Mahoney, M. J., & Howarth, N. 1992, *A&A*, 261, 47
- Kassim, N. E. 1989, *ApJ*, 347, 915
- Kettenis, M., van Langevelde, H. J., Reynolds, C., & Cotton, B. 2006, in *Astronomical Data Analysis Software and Systems XV*, eds. C. Gabriel, C. Arviset, D. Ponz, & S. Enrique, *ASP Conf. Ser.*, 351, 497
- Kronberg, P. P., Pritchett, C. J., & van den Bergh, S. 1972, *ApJ*, 173, L47
- Lacki, B. C. 2013, *MNRAS*, 431, 3003
- Lane, W. M., Cotton, W. D., van Velzen, S., et al. 2014, *MNRAS*, 440, 327
- Law, C. J., Yusef-Zadeh, F., & Cotton, W. D. 2008, *ApJS*, 177, 515
- Leahy, J. P., Muxlow, T. W. B., & Stephens, P. W. 1989, *MNRAS*, 239, 401
- Lenc, E., Garrett, M. A., Wucknitz, O., Anderson, J. M., & Tingay, S. J. 2008, *ApJ*, 673, 78
- Martí-Vidal, I., Marcaide, J. M., Alberdi, A., et al. 2011a, *A&A*, 526, A143
- Martí-Vidal, I., Marcaide, J. M., Alberdi, A., et al. 2011b, *A&A*, 533, A111
- McMullin, J. P., Waters, B., Schiebel, D., Young, W., & Golap, K. 2007, in *Astronomical Data Analysis Software and Systems XVI*, eds. R. A. Shaw, F. Hill, & D. J. Bell, *ASP Conf. Ser.*, 376, 127
- Moldón, J., Deller, A. T., Wucknitz, O., et al. 2015, *A&A*, 574, A73
- Morabito, L. K., Oonk, J. B. R., Salgado, F., et al. 2014, *ApJ*, 795, L33
- Muxlow, T. W. B., Beswick, R. J., Garrington, S. T., et al. 2010, *MNRAS*, 404, L109
- Nijboer, R. J., Pandey-Pommier, M., & de Bruyn, A. G. 2009, *SKA memo* 113, LOFAR imaging capabilities and system sensitivity
- Pérez-Torres, M. A., Lundqvist, P., Beswick, R. J., et al. 2014, *ApJ*, 792, 38
- Rau, U., & Cornwell, T. J. 2011, *A&A*, 532, A71
- Scaife, A. M. M., & Heald, G. H. 2012, *MNRAS*, 423, L30
- Thompson, A. R., Moran, J. M., & Swenson, G. W. 2001, *Interferometry and Synthesis in Radio Astronomy*, 2nd edn. (Weinheim: Wiley-VCH)
- Tully, R. B., Rizzi, L., Shaya, E. J., et al. 2009, *AJ*, 138, 323
- Unger, S. W., Pedlar, A., Axon, D. J., Wilkinson, P. N., & Appleton, P. N. 1984, *MNRAS*, 211, 783
- van Haarlem, M. P., Wise, M. W., Gunst, A. W., et al. 2013, *A&A*, 556, A2
- Weiler, K. W., & Sramek, R. A. 1988, *ARA&A*, 26, 295
- Weiler, K. W., Panagia, N., Montes, M. J., & Sramek, R. A. 2002, *ARA&A*, 40, 387
- Westmoquette, M. S., Smith, L. J., Gallagher, III, J. S., et al. 2009, *ApJ*, 696, 192
- Wills, K. A., Pedlar, A., Muxlow, T. W. B., & Wilkinson, P. N. 1997, *MNRAS*, 291, 517
- Wilson, T. L., Rohlf, K., & Hüttemeister, S. 2009, *Tools of Radio Astronomy* (Springer-Verlag)
- Wrobel, J. M., & Simon, R. S. 1986, *ApJ*, 309, 593
- Wucknitz, O. 2010a, in 10th European VLBI Network Symposium and EVN Users Meeting: VLBI and the New Generation of Radio Arrays
- Wucknitz, O. 2010b, in ISKAF2010 Science Meeting
- Xu, W., Readhead, A. C. S., Pearson, T. J., Polatidis, A. G., & Wilkinson, P. N. 1995, *ApJS*, 99, 297
- Yusef-Zadeh, F., & Morris, M. 1987, *ApJ*, 322, 721